Review Article

JRSM Cardiovascular Disease
Volume 7: 1–9

DOI: 10.1177/2048004018772237
journals.sagepub.com/home/cvd
SAGE

Magnetic resonance imaging: Physics basics for the cardiologist

Vassilios S Vassiliou[1,2], Donnie Cameron[2], Sanjay K Prasad[1] and Peter D Gatehouse[1]

Abstract

Magnetic resonance imaging physics can be a complex and challenging topic for the practising cardiologist. Its evolving nature and the increasing number of novel sequences used in clinical scanning have been topics of excellent reviews; however, the basic understanding of physics underlying the creation of images remains difficult for many cardiologists. In this review, we go back to the basic physics theories underpinning magnetic resonance and explain their application and use in achieving good quality cardiac imaging, whilst describing established and novel magnetic resonance sequences. By understanding these basic principles, it is anticipated that cardiologists and other health professionals will then appreciate more advanced physics manuscripts on cardiac scanning and novel sequences.

Keywords

Cardiology, cardiovascular imaging agents/techniques, computed tomography and magnetic resonance imaging, diagnostic testing

Introduction

In the last four decades, cardiovascular magnetic resonance (CMR) has become increasingly popular. It has been used to address complex clinical questions ranging from myocardial function, perfusion defects and viability, to quantification of valvular disease and identification and monitoring of shunts in congenital heart disease. CMR reports are a crucial aspect of practice for cardiologists and other health professionals such as cardiac surgeons and nurses; however, with the increasing complexity of CMR sequences, it is also less easy to follow and understand the physics underlying the new sequences. In this review, we revisit the basic physics principles underlying magnetic resonance imaging (MRI) and describe established and novel MRI pulse sequences. Once readers understand these basic physics principles, they will be able to appreciate further manuscripts describing advanced physics concepts.

History of magnetic resonance imaging

The fundamentals of MRI were laid down in the 1940s, when Felix Bloch proposed that atomic nuclei have properties that allow them to behave like tiny magnets.[1] He postulated that a charged particle spinning around its axis would have a magnetic field, or magnetic dipole moment, and published his theory in 1946. This theory was verified experimentally, and in the 1960s, nuclear magnetic resonance spectrometers were introduced; however, it took until the late 1970s for magnetic resonance to be applied clinically. Raymond Damadian proposed that the magnetic resonance properties of malignant tissue might differ from those of normal tissue,[2] and he produced an image of a tumour in a rat in 1974. In 1977, the first image of a human volunteer was acquired (Figure 1), requiring over 4 h of scanning. The word 'nuclear' was dropped around this time to avoid deterring patients from participating in this new form of imaging. Over time, MRI progressed from imaging static objects to moving

[1]Royal Brompton Hospital and Imperial College London, CMR Unit, London, UK
[2]Norwich Medical School, University of East Anglia, Bob Champion Research and Education, Norwich, UK

Corresponding author:
Vassilios S Vassiliou, Norwich Medical School, University of East Anglia, Floor 2, Bob Champion Research and Education, James Watson Road, Norwich NR4 7UQ, UK.
Email: v.vassiliou@rbht.nhs.uk

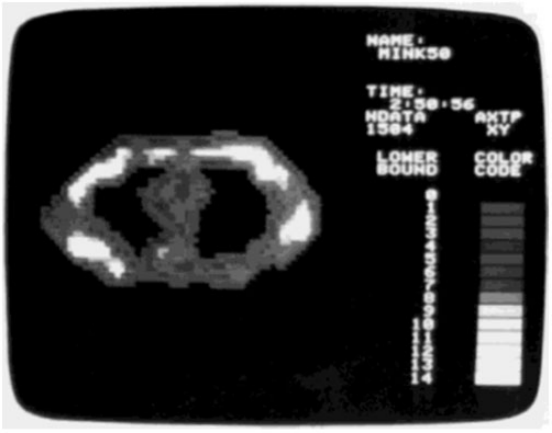

Figure 1. The first MRI image of the human body, obtained in 1977. Figure reproduced with permission from Basic MRI Physics by Blink.[3]

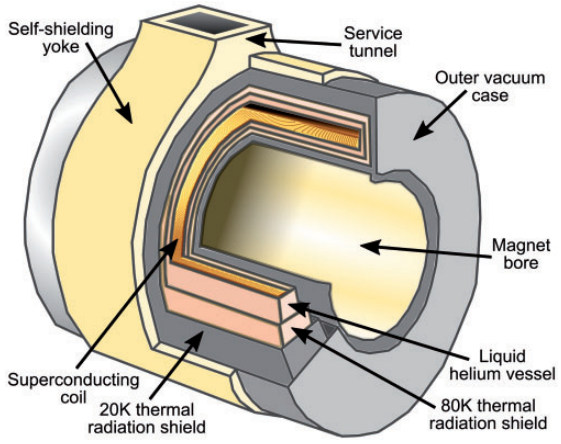

Figure 2. The components of a modern superconducting magnet. Multiple vacuum vessels surround the core, acting as temperature shields. These shields enable a slower boil off of the liquid helium. A cooling pump runs continuously aiming to almost eliminate the loss of helium.

objects, including the heart, with the aid of breath-holding techniques, or 'navigators' to monitor breathing motion. This enabled good quality anatomical imaging of the heart, and later led to functional imaging and myocardial tissue characterisation.

Essential MRI hardware

To enable MRI, the following specialised equipment is required, for further information see Supplementary material 1:

- *The magnet* – see Figure 2.
- *Radiofrequency chain*.
- *Shim coils*.

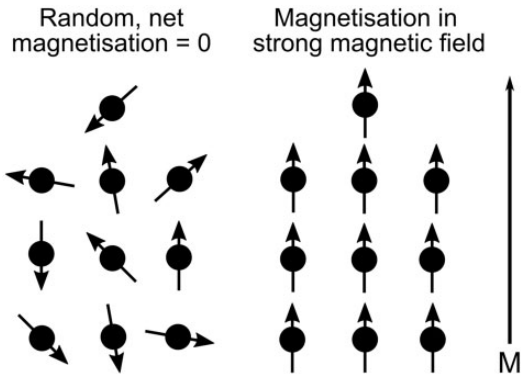

Figure 3. Each proton, depicted by , spins around a randomly oriented axis when there is no magnetic force, as shown on the left. Inside a strong magnetic field B, however, as shown on the right, protons tend to be pulled to align with the direction of the magnetic field because of their magnetic dipole moments, making the measurable but tiny nuclear magnetisation M that is used for MRI, and the associated spins therefore also tend to be aligned around that direction along the z axis.

- *Gradient coils*.
- *Computer hardware and software*.

Magnetic resonance imaging physics: Basic concepts

Our bodies are made of 80% water and each hydrogen atom in the water molecule has two subatomic particles, the nucleus called the proton (H^1) and an electron, with the proton being electrically charged (+1) and rotating around its own axis. The hydrogen atom is the most useful MRI source, as it is the most abundant element in the body. It is also the element with the highest gyromagnetic ratio, which is given as the ratio of its magnetic dipole moment to its angular momentum; this offers an advantage in MRI.

Other nuclei can be used for MRI and spectroscopy, such as: ^{13}C, ^{17}O, ^{19}F and ^{31}P.[4,5] All of these are currently used for research applications in CMR spectroscopy.[6,7]

Outside a magnetic field, the nuclei of hydrogen atoms are randomly oriented and provide a net magnetisation of zero (see Figure 3). However, when a subject is placed within a strong magnetic field, B_0, the nuclei tend to align in the direction of the field, producing a net magnetisation, M, along the z-axis, parallel to the scanner bore. This net magnetisation is then manipulated to generate images.

The Larmor frequency

When inside a magnet, the protons tend to align, as shown in Figure 3, and they also spin around their

own axes, since a spin combined with an electrical charge is classically viewed as having its own magnetic dipole moment, like a small bar magnet. Much like a gyroscope in a gravitational field, there is a fast spin; however, under the torque imposed by gravity, the gyroscope wobbles, or 'precesses', around the main gravitational field direction. This classical interpretation is not considered realistic on an individual nuclear spin scale; however, with enough nuclei considered together the classical model of a precessing magnetisation vector has been shown to be valid, and is known as the crowd behaviour model.[8]

The magnetisation within each microscopic volume containing crowd behaviour of protons can be modelled as precessing at the Larmor frequency, f, which is proportional to the gyromagnetic ratio, γ, and the magnetic field strength, B_0, as follows:

$$f = \gamma * B_0$$

This is useful as it allows us to calculate the operating frequency of the MRI system. For example, the Larmor frequency of a 1.5 T magnet is calculated like so:

$$\begin{aligned} &42.6(\text{gyromagnetic ratio of hydrogen in MHz/T}) \\ &\quad \times 1.5(\text{magnetic field strength in T}) \\ &= 63.9\,\text{MHz}(\text{Larmor frequency}) \end{aligned}$$

This is important as it is required for successful imaging, as discussed in the following section.

The term 'spin isochromat' is used to describe the magnetisation vector from a microsopic region showing uniform crowd behaviour; the term isochromat, or 'same colour', is used as all matter in the region has the same frequency of emission. Spin isochromat is abbreviated as 'spin' in most MRI literature, and this convention will be adopted henceforth in this review.

Resonance and excitation

The spins making up the net magnetisation vector have an angular precession rate, or frequency, and a phase, which describes the angular position relative to a fixed point. If, for example, two spins start from the same position but have slightly different frequencies, they will become out-of-phase, and this out-of-phase shift, or dephasing, will increase with time.

In preparation for scanning, the system measures the Larmor frequency of the water in the region of interest: namely, the thorax for cardiovascular applications. For further information, see Supplementary material 2.

Relaxation

By rotating the net magnetisation into the x–y plane (Figure 4), the constituent spins will also acquire energy from the radiofrequency (RF) pulse; however, the spins will gradually return to their original lower energy states, much like a basketball player jumping to put the ball in the basket will fall back to the ground soon after. This process of returning to the lower energy levels, to equilibrium, is called spin-lattice relaxation, or T_1.

T_1 relaxation. For the spins to return to equilibrium, the energy they have absorbed from the RF pulse must be released slowly back to their molecular environment. This manifests as a tiny amount of heat emission, but also partly as the emitted electromagnetic signal that is received for MRI. When the spins return to equilibrium, the excitation is essentially reset to zero, and the net magnetisation rotates back to align with the z-axis, B_0, as shown in Figure 4.

The recovery process is statistical over the crowd of protons, somewhat like radioactive decay but with no change in nuclear structure, only orientation, and a low energy of emission far short of ionisation at clinical magnetic field strengths. Not all protons are bound in their

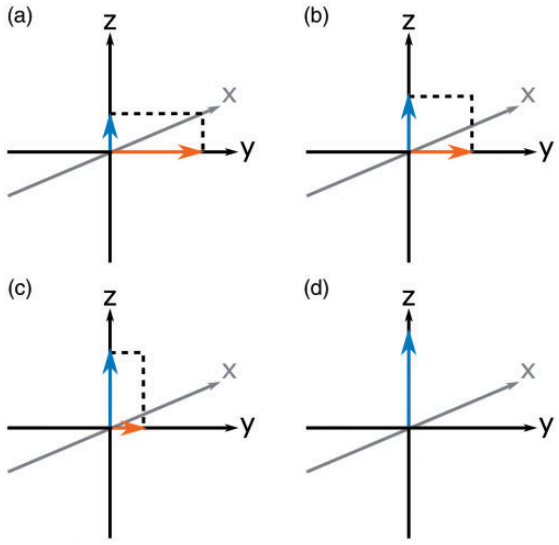

Figure 4. Following completion of the radiofrequency (RF) pulse, the net magnetisation will have moved to the x–y axis and then will start growing back on the z axis to return to equilibrium. So, the initial growth on the z axis (panel (a)) will be quickly succeeded by more growth (panel (b) and (c)) and the magnetisation will ultimately reach equilibrium (panel (d)), where all the magnetisation is along the z axis and there is no longer any magnetisation in the x–y plane. The T_1 parameter is also called longitudinal or spin-lattice relaxation, as most of the energy is released from the protons to the surrounding tissue; only a small fraction is emitted as the rotating electromagnetic field received for MRI.

molecules in the same way, and some will have tighter or weaker bonds than others; protons with tighter bonds will allow more rapid release of energy and will thus have a shorter T_1. This leads to an exponential rise to a maximum, familiar in physics (see Figure 5).

T_2 relaxation. The second type of relaxation is T_2 relaxation, a process independent of T_1 relaxation, but occurring simultaneously. While T_1 involves changes from the direction of the z-axis to the x–y plane, T_2 describes changes in the x–y plane. When the RF pulse is applied, the magnetisation transits into the x–y plane and the spins start to precess in phase; immediately after transmission of the RF pulse ends the net magnetisation vector, or transverse magnetisation, is rotating in the x–y plane around the z-axis, as shown in Figure 6(a). However, underlying this, the direct interaction between the spin magnetic dipole moments, known as 'spin-spin interaction', causes a submicroscopic dispersion in the apparent Larmor frequency of each spin isochromat, and the magnetisation vectors soon start to rotate at different rates (Figure 6(b)–(d)).

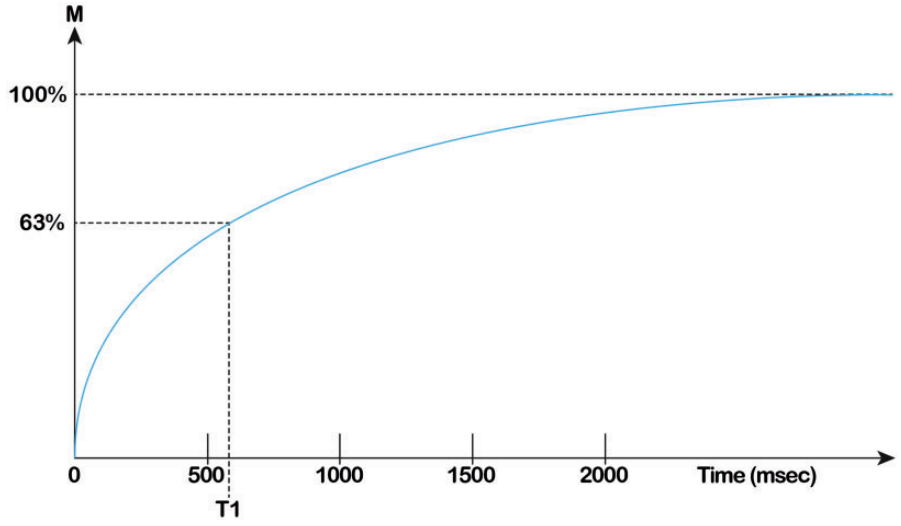

Figure 5. The T_1 relaxation curve. At time 0, immediately after the radiofrequency (RF) pulse, there is no magnetisation in the z direction. But immediately after, the z-axis magnetisation starts to recover. The parameter T_1 is defined as the time required for the longitudinal magnetisation to reach 63% of the initial magnetisation. It is interesting to appreciate that this was the principle upon which Damadian based his initial MR work in realising that some tumours may have a higher T_1 than normal tissue.[2]

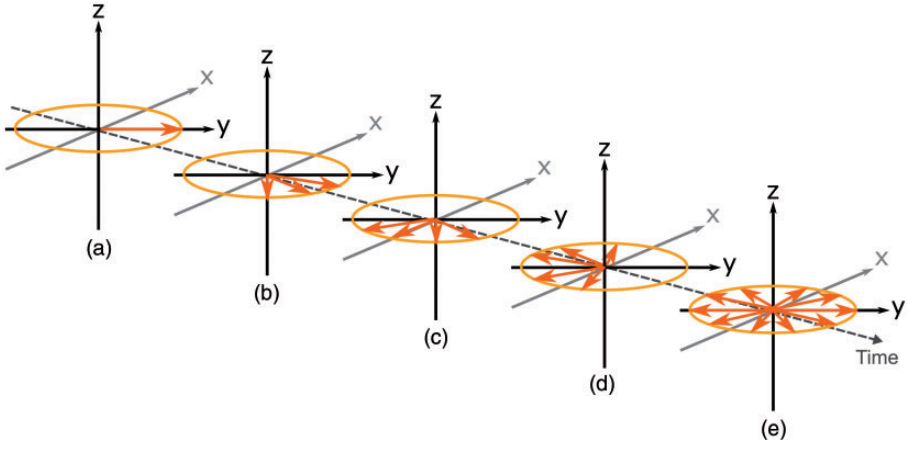

Figure 6. The process of T_2 relaxation following a radiofrequency pulse. All the vectors have different speeds and soon start pointing in different directions (panels (a)–(d)). Although all protons are rotating around the z axis in the x–y plane, with time all vectors now point in different directions (panel (e)). The process of transforming from totally in-phase, where all vectors align together, to totally out-of-phase, where no vector is aligned together, is called T_2 relaxation, whilst the total signal from all these vectors pointing in different directions is near-zero.

Like T_1 relaxation, T_2 relaxation causes a decaying effect, but this time in the available transverse magnetisation detected by the receiver coil (see Figure 7).

Two physical reasons exist for the decay of the total received M_{xy} signal: the spins may dephase relative to each other due to genuine spin-spin interactions (T_2), or because they are in different magnetic field strengths and are therefore precessing at different frequencies (T_2 prime, or T_2'). The T_2' effect applies on a macroscopic scale, over the entirety of the patient, down to subvoxel scale, due to excessive iron in tissues, for example. Its impact is highly dependent on the physical distance scale in question. The combined dephasing effect of T_2 and T_2' is known as T_2*, or T_2 star, where T_2' is usually but not always faster than T_2.

Image acquisition

During relaxation following the RF pulse, the protons release their excess energy, partly as RF waves. These waves must be captured in order to produce an image, and this is achieved using a receiver coil, which is sometimes the same as the transmission coil. For safety, the transmission coil is typically housed at a distance from the patient, as it carries peak RF powers in the region of 10,000 W in short pulses, which might become dangerous. The receiver coil must also be positioned at or near right angles to B_0, as the precessing magnetisation has an oscillating M_{xy} component only, which generates a weak oscillating magnetic field in the x–y plane.

Image creation and display

As shown in Figure 8, the RF pulse causes excitation, followed by precession and relaxation, and from this the RF waves are picked up by the receiver and fed into a computer to produce an image.

The fundamental principle that makes a projection or one-dimensional image of the patient can be imagined as follows. When a signal is received in the presence of a gradient applied across the excited slice, it contains high frequencies from one side of the patient and low frequencies from the other. We can analyse the spectrum of this signal by performing Fourier transformation, and this tells us how much tissue is at each position across the magnet in the direction of the applied gradient. This is called frequency encoding of position.

We repeat this process, each time with a further 'twist' of signal phase along the other in-plane direction, the phase-encoding direction, to assemble a frequency slope over the repeated steps. Further spectrum analysis can then be performed to give positional information in the phase-encode direction.

Basic cardiovascular magnetic resonance pulse sequences

Spin echo

Spin echo pulse sequences acquire images during one fixed phase of the cardiac cycle, the timing of which is governed by a triggering delay after the R-wave. Following the initial 90° RF pulse, the net

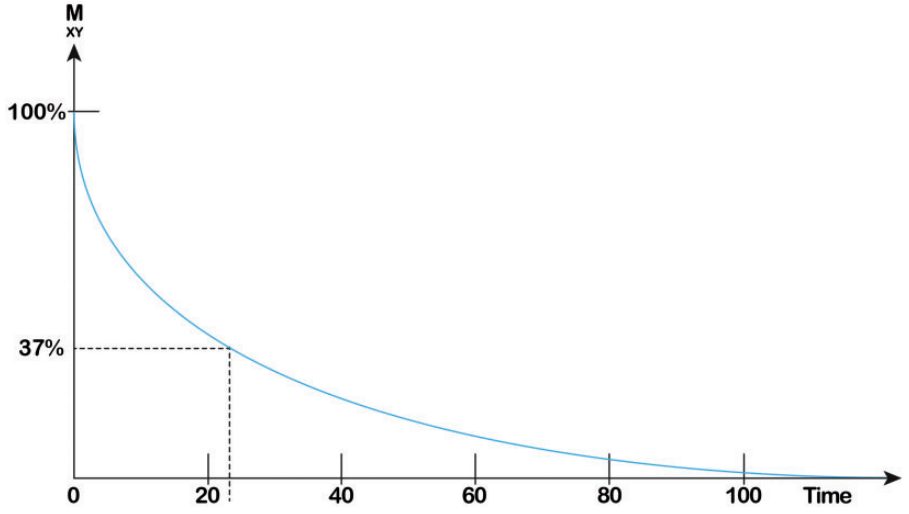

Figure 7. A T_2 relaxation curve. Following the 90° radiofrequency (RF) pulse, all the magnetisation flips into the x–y plane where it is labelled M_{xy}. Initially all the spins are in the same phase; however, immediately after the RF pulse they start to become out of phase. T_2 is the time taken for the total signal to decay to 37% of the original value. T_2 usually occurs much faster than T_1 and it is also called spin-spin relaxation as it describes interactions between the protons. Once both T_1 and T_2 relaxation processess are finished the original equilibrium is restored along the main magnetic field (B_0).

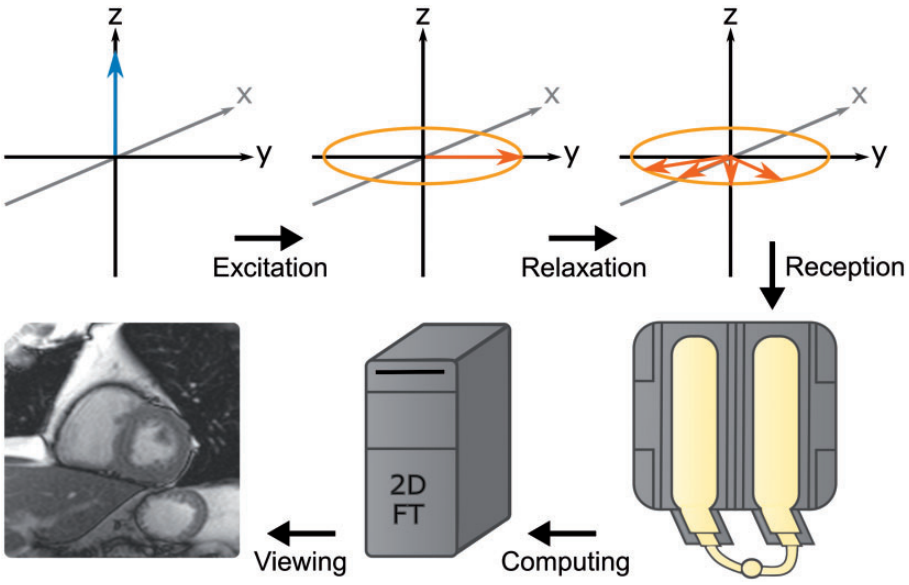

Figure 8. A flowchart describing the process from sending the radiofrequency (RF) pulse to viewing the image. Nowadays, the computing is based on a two-directional frequency analysis known as the 2D Fourier transform. A computing method for high speed known as fast Fourier transform (FFT) was essential in the early days of MRI;[9] however, this is no longer important in view of the strong computing power that allows even a simple program for the Fourier Transform to be fast enough for images to appear almost instantly after data collection ends.

magnetisation starts to dephase due to T_2* relaxation. Then a second RF pulse at 180° follows, causing the protons to rephase the T_2' contribution of main field non-uniformity at the 'echo time', recovering the inhomogeneous dephasing to leave pure T_2 decay. Spin echo images can have both T_1- and T_2-weighted properties: T_2 weighting increases with longer echo times while T_1 weighting occurs if the 90–180° acquisition process is repeated before complete T_1 recovery has occurred. To minimise T_1 weighting, it is necessary to pause the pulse sequence so that it acquires only every second or third cardiac cycle, depending on the patient's heart rate. Clinical applications of the spin echo sequence include: obtaining anatomical information, where blood appears darkened by a flow-dependent preparation method;[10] imaging for myocarditis, pericarditis, cardiomyopathies, vasculitis and cardiac tumours; and assessing myocardial scar following gadolinium contrast administration.[11,12]

Cine imaging sequences

Gradient echo, or gradient recalled echo (GRE), imaging is based on a single RF pulse, typically <90°, avoiding the additional time and motion sensitivity of a spin echo 180° RF pulse. This sequence can be repeated continuously, delivering an apparent functional cine of the cardiac cycle. This is performed using a standard gradient echo pulse sequence or a steady-state free-precession (SSFP) sequence, which provides more reliable contrast between blood and myocardium due to the markedly longer T_2 of blood than myocardium. To complete imaging within a breath-hold, multiple lines of the raw data are collected within each cardiac cycle: this is especially useful for cardiac imaging of the fast pumping heart, as it enables apparent dynamic cine imaging, which is essentially a video of the heart pumping from diastole to systole. It should be noted that the images are assembled over multiple cycles under the assumptions of adequate breath-holding and reliable ECG detection in normal rhythm. Thanks to these features, cine CMR delivers the reference standard estimation for atrial and ventricular volumes and ejection fraction.

Late gadolinium enhancement imaging

Late gadolinium enhancement (LGE) imaging is highly T_1-sensitive gradient-echo imaging undertaken after the administration of a gadolinium-based contrast agent (Gd), which distributes in greater volumes in fibrotic myocardium, where it demonstrates slower washout times compared to normal myocardium. Using a T_1-sensitive gradient echo sequence, usually 10–15 min after the administration of Gd, it is possible to demonstrate the abnormal deposition of the contrast agent late after injection: focal regions of fibrosis become enhanced, indicating replacement fibrosis,[13–16] whereas normal myocardium remains black. Expertise is needed to adjust the inversion–recovery null time so

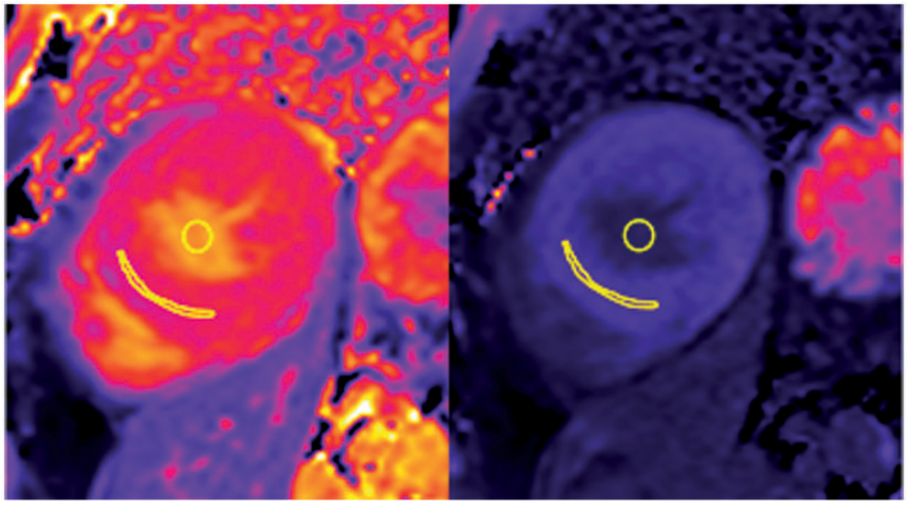

Figure 9. Native and post-gadolinium (Gd) T_1 maps. Using the native and post Gd T_1 values for blood and myocardium, and incorporating haematocrit, the extracellular volume fraction (ECV) can be calculated for the corresponding slice location with the formula described in the text. The yellow crescent and circle represent the regions of interest from which T_1 values are measured, in the myocardium and blood pool, respectively.

that normal myocardium is nulled and appears dark, on the assumption that the disease sought has a focal or localised pattern of distribution in the myocardium. LGE has been a milestone in CMR, as the presence of enhancement indicating various kinds of focal fibrosis has been validated histologically, and has been shown to be associated with higher risk of worse outcome in a plethora of conditions including dilated cardiomyopathy,[17,18] valve disease[19] and hypertrophic cardiomyopathy.[20]

Myocardial T_1 and T_2 mapping

Recently there has been considerable interest in new myocardial tissue characterisation techniques such as T_1 and T_2 mapping, which are increasingly used in research and clinical practice.[21,22] It is therefore important to comment on this topic in this review, and to explain the utility of these relatively novel imaging methods.

Myocardial T_1 mapping. Although LGE is validated for identification of focal fibrosis, it relies on clear distinction between normal and abnormal myocardial tissue in order to be sensitive to abnormalities. Therefore, a clinical need arose to have an imaging biomarker that could identify subtle diffuse, 'interstitial' fibrosis as opposed to the more definite focal, 'replacement' fibrosis. A clinically applicable method of myocardial single-breath-hold T_1-mapping, known as MOdified Look-Locker Imaging or MOLLI,[23] has been introduced as a surrogate measure of interstitial fibrosis, and similar methods have shown good correlation with histologically identified collagen volume fraction.[24]

MOLLI is ECG triggered and all images are acquired in late diastole.[25] The original MOLLI sequence acquired 11 inversion–recovery images over 17 heart beats, and therefore was of limited use in patients who could not perform a good breath hold. Newer sequences obtain 8 inversion–recovery images in 11 heart beats, in a single breath hold of 8–12 s depending on the heart rate of the patient. MOLLI is based on multiple inversion recovery images acquired both before and after contrast administration. Following motion correction and co-registration, a T_1 map is derived via pixel-wise curve fitting (see Figure 9), allowing segmental analysis of T_1 values. Native and post Gd images can be used, and with the addition of haematocrit measurements the extracellular volume fraction can be derived as follows:

$$ECV = \frac{(1 - \text{haematocrit}) * \left(\frac{1}{T_1\text{myopost}} - \frac{1}{T_1\text{myopre}}\right)}{\left(\frac{1}{T_1\text{bloodpost}} - \frac{1}{T_1\text{bloodpre}}\right)}$$

where ECV = extracellular volume fraction, T_1 myo = myocardial T_1, T_1 blood = blood T_1, pre = native T_1, post = following Gd administration. The multiplication by (1 − haematocrit) represents the blood volume of distribution and converts the equation to myocardial ECV from partition coefficient;[25] this has proved useful in cardiomyopathies,[26] valve disease[27] and myocardial infarction.[28]

Myocardial T_2 mapping. Today, T_2-weighted spin-echo methods are popular for assessing pathologies such as acute myocardial infarction and myocarditis.[29] These techniques are qualitative, and are subject to pitfalls such as poor signal-to-noise and artefacts relating to coil sensitivity variations,[30] slow-flowing blood adjacent to hypokinetic myocardium and poor pulse sequence timing relative to the cardiac cycle. To mitigate these problems, quantitative T_2 mapping techniques have been proposed.[29] These are similar to T_1 mapping techniques in that several T_2-weighted images are acquired in the same cardiac phase over multiple heartbeats, and pixelwise curve fitting is performed to visualise the variation of T_2 across the myocardium. This method proves particularly useful for imaging myocardial oedema associated with inflammation; however, it does not have the diverse applications of T_1 mapping, and is thus less-frequently used.

Cardiovascular magnetic resonance safety considerations

In terms of imaging examinations, CMR is thought to be a safe test, since it does not apply ionising radiation. As such it is free from concerns about neoplasia associated with other forms of imaging such fluoroscopically guided invasive cardiac angiography and computed tomography; however, there are cautions and contraindications to CMR, relating to the paramagnetic agents used, patients with implantable devices and some more recent concerns regarding a theoretical association with neoplasia. These are discussed further in Supplementary material 3.

Conclusion

Modern CMR machines have evolved and improved considerably, allowing faster and better imaging, but many of the fundamental principles behind MR scanning have remained the same since the late 1970s. Well-established sequences for cardiac anatomy and function have been complemented by myocardial tissue characterisation with LGE, and are now further supplemented with T_1 mapping towards more complete phenotypic characterisation of patients, providing diagnostic and prognostic information. This review has offered a summary of these methods, providing the reader with a gateway to more detailed articles.

Declaration of conflicting interests

The author(s) declared no potential conflicts of interest with respect to the research, authorship, and/or publication of this article.

Funding

The author(s) disclosed receipt of the following financial support for the research, authorship, and/or publication of this article: Dr Vassiliou and Dr Prasad have been partially supported by the Rosetrees Charity Trust.

Ethical approval

None.

Guarantor

Dr Vassiliou is the Guarantor.

Contributorship

Dr Prasad and Dr Gatehouse contributed equally. Dr Vassiliou wrote the first draft, all other authors made significant contributions and approved the final manuscript. No Ethical approval required.

References

1. Bloch F, Hansen W and Packard M. Nuclear induction. *Phys Rev* 1946; 69: 127–129.
2. Damadian R. Tumor detection by nuclear magnetic resonance. *Science* 1971; 171: 1151–1153.
3. Blink E. Basic MRI physics, 2004, pp. 1–76, www.mriphysics.net (accessed 15 July 2017).
4. Dehghani MM, Lanz B, Duarte JMN, et al. Refined analysis of brain energy metabolism using in vivo dynamic enrichment of 13C multiplets. *ASN Neuro* 2016; 8: pii: 1759091416632342. doi: 10.1177/1759091416632342.
5. Atkinson IC, Sonstegaard R, Pliskin NH, et al. Vital signs and cognitive function are not affected by 23-sodium and 17-oxygen magnetic resonance imaging of the human brain at 9.4 T. *J Magn Reson Imag* 2010; 32: 82–87.
6. Mahmod M, Francis JM, Pal N, et al. Myocardial perfusion and oxygenation are impaired during stress in severe aortic stenosis and correlate with impaired energetics and subclinical left ventricular dysfunction. *J Cardiovasc Magn Reson* 2014; 16: 29.
7. Tyler DJ and Neubauer S. Science to practice: hyperpolarized metabolic MR imaging: the light at the end of the tunnel for clinical (13)C MR spectroscopy? *Radiology* 2016; 278: 639–641.
8. Tomonaga S-I and Oka T. *The story of spin*. Chicago: University of Chicago, 1997.
9. Shenberg I and Macovski A. Applications of time-varying gradients in existing magnetic resonance imaging systems. *Med Phys* 1986; 13: 164–169.
10. Geva T, Vick GW, Wendt RE, et al. Role of spin echo and cine magnetic resonance imaging in presurgical planning of heterotaxy syndrome. Comparison with echocardiography and catheterization. *Circulation* 1994; 90: 348–356.
11. Mitchell FM, Prasad SK, Greil GF, et al. Cardiovascular magnetic resonance: diagnostic utility and specific considerations in the pediatric population. *WJCP* 2016; 5: 1–15.

12. Jung BA and Weigel M. Spin echo magnetic resonance imaging. *J Magn Reson Imag* 2013; 37: 805–817.
13. Amado LC, Gerber BL, Gupta SN, et al. Accurate and objective infarct sizing by contrast-enhanced magnetic resonance imaging in a canine myocardial infarction model. *J Am Coll Cardiol* 2004; 44: 2383–2389.
14. Harris MA, Johnson TR, Weinberg PM, et al. Delayed-enhancement cardiovascular magnetic resonance identifies fibrous tissue in children after surgery for congenital heart disease. *J Thorac Cardiovasc Surg* 2007; 133: 676–681.
15. Vassiliou VS, Flynn PD, Raphael CE, et al. Lipoprotein (a) in patients with aortic stenosis: insights from cardiovascular magnetic resonance. Cheng X (ed). *PLoS One* 2017; 12: e0181077.
16. Vassiliou VS, Perperoglou A, Raphael CE, et al. Midwall fibrosis and 5-year outcome in patients with moderate and severe aortic stenosis. *J Am Coll Cardio* 2017; 69: 1755–1756.
17. Gulati A, Jabbour A, Ismail TF, et al. Association of fibrosis with mortality and sudden cardiac death in patients. *J Am Med Assoc* 2013; 309: 6896–6908.
18. Halliday BP, Gulati A, Ali A, et al. Association between midwall late gadolinium enhancement and sudden cardiac death in patients with dilated cardiomyopathy and mild and moderate left ventricular systolic dysfunction. *Circulation* 2017; 135: 2106–2115.
19. Dweck MR, Joshi S, Murigu T, et al. Midwall fibrosis is an independent predictor of mortality in patients with aortic stenosis. *J Am Coll Cardiol* 2011; 58: 1271–1279.
20. Chan RH, Maron BJ, Olivotto I, et al. Prognostic value of quantitative contrast-enhanced cardiovascular magnetic resonance for the evaluation of sudden death risk in patients with hypertrophic cardiomyopathy. *Circulation* 2014; 130: 484.
21. Vassiliou V, Wassilew K, Cameron D, et al. Identification of myocardial diffuse fibrosis by 11 heartbeat MOLLI T1 mapping: averaging to improve precision and correlation with collagen volume fraction. *MAGMA* 2018; 31: 101–11.
22. Cameron D, Vassiliou VS, Higgins DM, et al. Towards accurate and precise T 1 and extracellular volume mapping in the myocardium: a guide to current pitfalls and their solutions. *Magn Reson Mater Phy* 2018; 31: 143–163.
23. Messroghli DR, Radjenovic A, Kozerke S, et al. Modified look-locker inversion recovery (MOLLI) for high-resolution T1 mapping of the heart. *Magn Reson Med* 2004; 52: 141–146.
24. Flett AS, Hayward MP, Ashworth MT, et al. Equilibrium contrast cardiovascular magnetic resonance for the measurement of diffuse myocardial fibrosis: preliminary validation in humans. *Circulation* 2010; 122: 13138–13144.
25. Kellman P, Wilson JR, Xue H, et al. Extracellular volume fraction mapping in the myocardium, part 1: evaluation of an automated method. *J Cardiovasc Magn Reson* 2012; 14: 63.
26. Nyktari E, Vassiliou VS, Arzanauskaite M, et al. Challenging Occam's razor: an unusual combination of sarcoidosis and amyloidosis. The value of CMR in infiltrative cardiomyopathies. *Can J Cardiol*. 2017; 33: 1335. e9–1335.
27. Chin CWL, Everett RJ, Kwiecinski J, et al. Myocardial fibrosis and cardiac decompensation in aortic stenosis. *JACC Cardiovasc Imag* 2017; 10: 1320–1333.
28. Bulluck H, Bryant JA, Lim MX, et al. Full left ventricular coverage is essential for the accurate quantification of the area-at-risk by T1 and T2 mapping. *Sci Rep* 2017; 7: 4871.
29. Giri S, Chung Y-C, Merchant A, et al. T2 quantification for improved detection of myocardial edema. *J Cardiovasc Magn Reson* 2009; 11: 56.
30. Keegan J, Gatehouse PD, Prasad SK, et al. Improved turbo spin-echo imaging of the heart with motion-tracking. *J Magn Reson Imag* 2006; 24: 563–570.